Multiscale Variabilities in Global Sea Surface Temperatures and Their Relationships with Tropospheric Climate Patterns

DAVID B. ENFIELD

NOAA/Atlantic Oceanographic and Meteorological Laboratory, Miami, Florida

ALBERTO M. MESTAS-NUÑEZ

Cooperative Institute for Marine and Atmospheric Studies, University of Miami, Miami, Florida

ABSTRACT

El Niño–Southern Oscillation (ENSO) is a global phenomenon with significant phase propagation within and between basins. This is captured and described in the first mode of a complex empirical orthogonal function (CEOF) analysis of sea surface temperature anomaly (SSTA) from the midnineteenth century through 1991. The global ENSO from the SSTA data, plus a linear trend everywhere, are subsequently removed in order to consider other global modes of variability uncontaminated by the intra- and interbasin effects of ENSO. An ordinary EOF analysis of the SSTA residuals reveals three non-ENSO modes of low-frequency variability that are related to slow oceanic and climate signals described in the literature. The first two modes have decadal to multidecadal timescales with high loadings in the Pacific. They bear some spatial similarities to the ENSO pattern but are broader, more intense at high latitudes, and differ in the time domain. A CEOF analysis confirms that they are not merely the phase-related components of a single mode and that all three modes are without significant phase propagation. The third mode is a multidecadal signal with maximal realization in the extratropical North Atlantic southeast of Greenland. It is consistent with studies that have documented connections between North Atlantic SSTA and the tropospheric North Atlantic Oscillation (NAO).

All three SSTA modes have midtropospheric associations related to previously classified Northern Hemisphere teleconnection patterns. The relationships between SSTA modes and tropospheric patterns are consistent with the ocean–atmosphere interactions discussed in previous studies to explain low-frequency climate oscillations in the North Pacific and North Atlantic sectors. The first three leading modes of non-ENSO SSTA are most related, to the tropospheric patterns of the Pacific North American, the North Pacific, and the Arctic oscillations (AO), respectively. The 500-hPa pattern associated with the third SSTA mode also bears similarities to the NAO in its Atlantic sector. This North Atlantic mode has a region of high, positive SSTA loadings in the Gulf of Alaska, which appear to be connected to the North Atlantic SSTA by a tropospheric bridge effect in the AO.

1. Introduction

After the annual cycle, the Pacific El Niño–Southern Oscillation (ENSO) and its climatic impacts around the world constitute the strongest, most globally coherent climate signal that exists in both the ocean and the atmosphere. Coupled ocean–atmosphere models developed in the past 15 years have demonstrated the potential for prediction of ENSO-related Pacific sea surface temperature (SST) fluctuations (Barnston et al. 1994). However, the numerical prediction of anomalous SST (SSTA) variability in other oceans and the impact of ocean–atmosphere interactions on precipitation are not

yet within reach and may require at least another decade of research. To get beyond the mere prediction of equatorial Pacific ''warm events,'' value-added forecasts of land precipitation based on global numerical SSTA predictions and the empirical relationships between rainfall and SSTA must become a future norm.

An attractive way to mine the untapped predictability in the ocean–atmosphere system is to predict SSTA in other ocean basins at useful lead times of one to several seasons, and utilize its empirical associations with climate departures, especially for rainfall. Most, but not all, of the SSTA variability outside of the tropical Pacific is not related to ENSO, is less well understood, and is presently unpredictable with operational methods. However, ENSO-related variability does occur outside of the core region of the tropical Pacific where the coupled interactions responsible for ENSO occur. This more passive extraregional variability can complicate efforts to understand the effects of non-ENSO variability. One can,

Corresponding author address: Dr. David B. Enfield, NOAA/Atlantic Oceanographic and Meteorological Laboratory, 4301 Rickenbacker Causeway, Miami, FL 33149.
E-mail: enfield@aoml.noaa.gov

of course, use the leading mode of an empirical orthogonal function (EOF) analysis to represent ENSO and restrict attention to the other modes. Cane et al. (1997) adopted a similar approach to isolate century-scale trends from the effects of low-frequency changes associated with ENSO behavior. However, because the extraregional ENSO variability has a significant lagged component (e.g., Latif and Barnett 1996; Enfield and Mayer 1997) that cannot be adequately represented in the primary mode of an ordinary EOF analysis, significant ENSO "contamination" of the non-ENSO modes will occur.

In this paper we present an analysis of more than a century of global SSTA, separating its nonseasonal variability into ENSO and non-ENSO components using a complex variant of EOF analysis that avoids the problem of lagged variability. After first describing the extracted global ENSO component, we then focus on several globally distributed non-ENSO modes whose strongest variability lies outside of the tropical Pacific and at longer than interannual timescales. We also examine their relationships with midtropospheric pressure height variability and compare them with previous findings about climate variability.

2. Data and methods

A global SSTA dataset is required because the non-ENSO variability is globally distributed and because tropospherically connected ENSO signals occur elsewhere in the World Ocean (Covey and Hastenrath 1978; Hastenrath et al. 1987; Latif and Barnett 1995; Tourre and White 1995; Lanzante 1996; Enfield and Mayer 1997) and also affect world climate (Lau and Nath 1994). The dataset should also have a century scale to detect secular trends and resolve decadal to multidecadal fluctuations. The 1856–1991 monthly reconstruction of historical ship-based data by Kaplan et al. (1998, henceforth K98) on a $5° \times 5°$ global grid is ideally suited for both requirements. The K98 analysis uses the covariance structure of the global SSTA field to fill missing data in a statistically optimal way. It reconstructs the data based on the first 80 empirical modes of the modern portion of the data record in a manner analogous to that of Smith et al. (1996) but uses inverse modeling techniques to reconstruct the older observations. Such reconstructions are not well suited to analysis on small regional scales because they smooth out the variability at high frequencies and wavenumbers. However, for the basinwide scales typical of ENSO and interdecadal variability they pose special advantages, especially for early periods that were more sparsely sampled than the modern era.

The K98 data are first smoothed with a low-pass filter that eliminates periodicities of 1.5 yr or less. The smaller timescales eliminated include intraseasonal and month-to-month variations associated with the smaller regional space scales for which the reconstructed data are less appropriate. For the calculation of the global ENSO component, we apply an additional high-pass filter to temporally remove periodicities longer than 8 yr, yielding a 1.5–8 yr passband for that component. We subsequently remove the ENSO component from the smoothed K98 (not the bandpassed) data, whereby the residuals contain non-ENSO variability at all periodicities longer than 1.5 yr.

To account for the phase propagations in the ENSO mode as well as in the non-ENSO modes (if they occur), we perform a standard eigenvector decomposition on a transformed, complex dataset in which the real part is composed of the bandpassed K98 data and the imaginary part of its Hilbert transform. The standard EOF procedure applied to the complex data then yields a complex EOF result (CEOF) in which spatial and temporal phase information is preserved in the ENSO-related first mode (Rasmusson et al. 1981). Lanzante (1996) has used a very similar approach to analyze the amplitude and phase structure of the ENSO mode in the global Tropics for the 1875–1979 time period but without first eliminating decadal and longer timescales (our 8-yr filter). In the last step of our data preparation the first (global ENSO) CEOF mode realization at every grid point is then removed from the 1.5-yr filtered K98 data to form a residual dataset for the analysis of long timescale (non-ENSO) modes.

Enfield and Mestas-Nuñez (1999) recently did a similar analysis of the K98 data residuals in which they did not eliminate trends. Almost all of the secular variation emerged in the first mode of residual variability and was superimposed on energetic interdecadal fluctuations with a similar spatial amplitude distribution. Because in this paper we wish to isolate the interdecadal signal from the secular variation, we have first detrended the residual K98 data at every grid point. The detrending approach of Zhang et al. (1997) consists of subtracting the global mean from each monthly SSTA map. This procedure was not followed here because regional trends remain that obscure the interdecadal variability on smaller scales. Figure 1 shows the global distribution of the removed trends, which is seen to be very similar to the spatial amplitudes of the first non-ENSO CEOF of Enfield and Mestas-Nuñez (1999, their Fig. 3b).

To represent the midtropospheric circulation of the Northern Hemisphere we use the monthly 500-hPa pressure heights on a 47×51 polar stereographic grid. These data were obtained from the data archive of the National Center for Atmospheric Research and cover the period 1955–97. Departures of the 500-hPa data from their mean annual cycle are composited with respect to the positive and negative phases of the reconstructed temporal realizations for the non-ENSO SSTA modes.

3. The global ENSO in SST

We show the spatial amplitude, spatial phase, and temporal realization of the first global CEOF mode in Fig. 2. The mode explains 34.4% of the global variance in the bandpassed data and 17% in the low-passed data
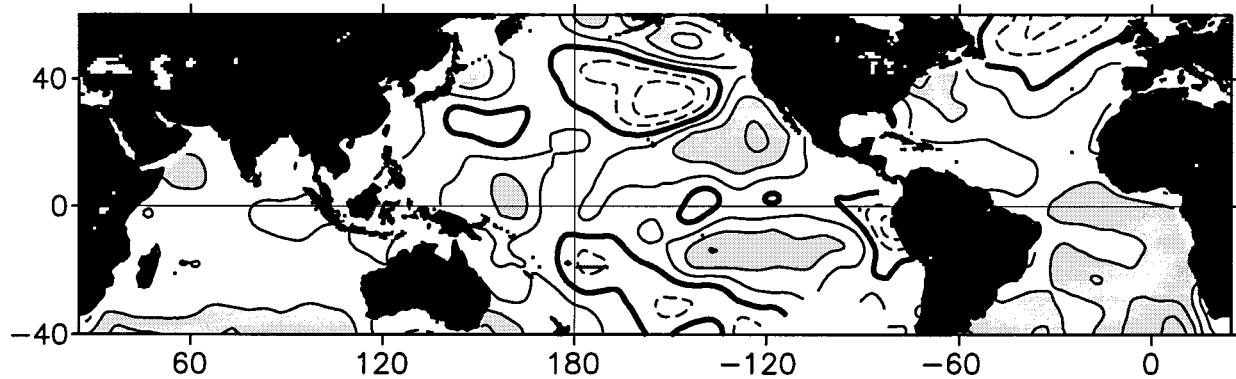
FIG. 1. Distribution of the 1856–1991 linear (least squares) trend (°C century^{-1}) in the smoothed Kaplan et al. (1998) SSTA dataset. The contour interval is 0.2°C century^{-1}, the heavy contour is zero, and the light solid (dashed) contours are positive (negative).

(the latter includes decadal to multidecadal variabilities). The local explained variance in the regions of high (low) amplitudes (upper panel) are of course much larger (smaller) than the global amount.

To represent the temporal behavior of the mode (bottom panel), we show the temporal reconstruction (temperature units) for phases and amplitudes combined over an index region rather than the more confusing temporal amplitude and phase functions from which they are derived (i.e., the complex expansion coefficients for the mode). The obvious reference rectangle to use for the ENSO mode is the well-known NINO3 region in the equatorial Pacific, bounded by 5°N–5°S, 90°–150°W (middle panel). The modal time variability elsewhere is merely the same series lagged by the appropriate spatial phase (middle panel) and with amplitude attenuated in proportion to the spatial amplitude (upper panel).

Rather than show the spatial amplitude in arbitrary CEOF units, we display the geographic distribution of the gain with respect to the modal variability over the reference rectangle (upper panel). We define the gain as the ratio of the mode amplitude at any grid point to the mean amplitude in the NINO3 region. Thus, a contour value of 30 indicates regions where the amplitude of the mode is 30% of the mean amplitude in the NINO3 region, where the gain is 100%. Significance tests on the correlation coefficients between the data and the temporal reconstruction show that amplitudes in the white regions (<10) are insignificant.

For ease of display, the spatial phase (middle panel) has been transformed into a temporal lag at each grid point (units of 3-month seasons), referenced to the NINO3 phase at a nominal midband periodicity. That periodicity is 43.7 months, based on the 37 zero upcrossings in the 135-yr modal time series (bottom panel). This is about midway in the 3–4-yr range usually attributed to ENSO variability and corresponds to eight degrees of spatial phase per month of lag. The average lag in the NINO3 region is zero.

The temporal reconstruction shown in Fig. 2 is not simply a smoothed version of an index obtained by av-

eraging the monthly data over the NINO3 region. It is the average over the NINO3 region of the SSTA reconstructed from the ENSO mode. It is therefore the ENSO mode contribution to the usual data-derived version of the NINO3 index and as such it has some differences with respect to the latter. Notice, for example, that the 1982–83 warm event (El Niño) is not the strongest ENSO fluctuation in the record, as a similarly filtered average of the SSTA data would show. That is because part of that event's amplitude is actually in the slowly varying background state that was warm during the 1980s. In 1983 that background condition is captured by two of the slower non-ENSO modes discussed in the next section.

The spatial functions show the classic features normally associated with ENSO in the Pacific: 1) a region of intense amplitude within ±10° of the equator and east of the date line, decreasing to smaller amplitudes over a wide, wedge-shaped region that spreads poleward along the eastern boundary; 2) phase propagation northward along the coast of North America, with maximum lags of one to two seasons in the Gulf of Alaska and the Bering Sea; and 3) regions of intermediate amplitude and opposite phase in the central North Pacific (30°–45°N) and the central South Pacific (20°–40°S). Less documented features include 4) one-season lags in the central Pacific near ±20°, and 5) a precursor off central Chile with a one-season lead. Although a large region of the southeast (SE) Pacific has few data (unshaded area, offshore), the latter feature lies along the coastal ship route north of Cape Horn that has been relatively well sampled since the nineteenth century. Moreover, Rasmusson and Carpenter (1982) have previously mentioned this precursor. A possible cause of the precursor is a weakening in the SE trades (and associated surface heat fluxes) off Chile, prior to the main trade wind weakening at lower latitudes.

Both the tropical Atlantic and Indian Oceans show known coherence and lag structures relative to the equatorial Pacific. The tropical Atlantic is lagged by one to three seasons with phase propagation toward the equa-
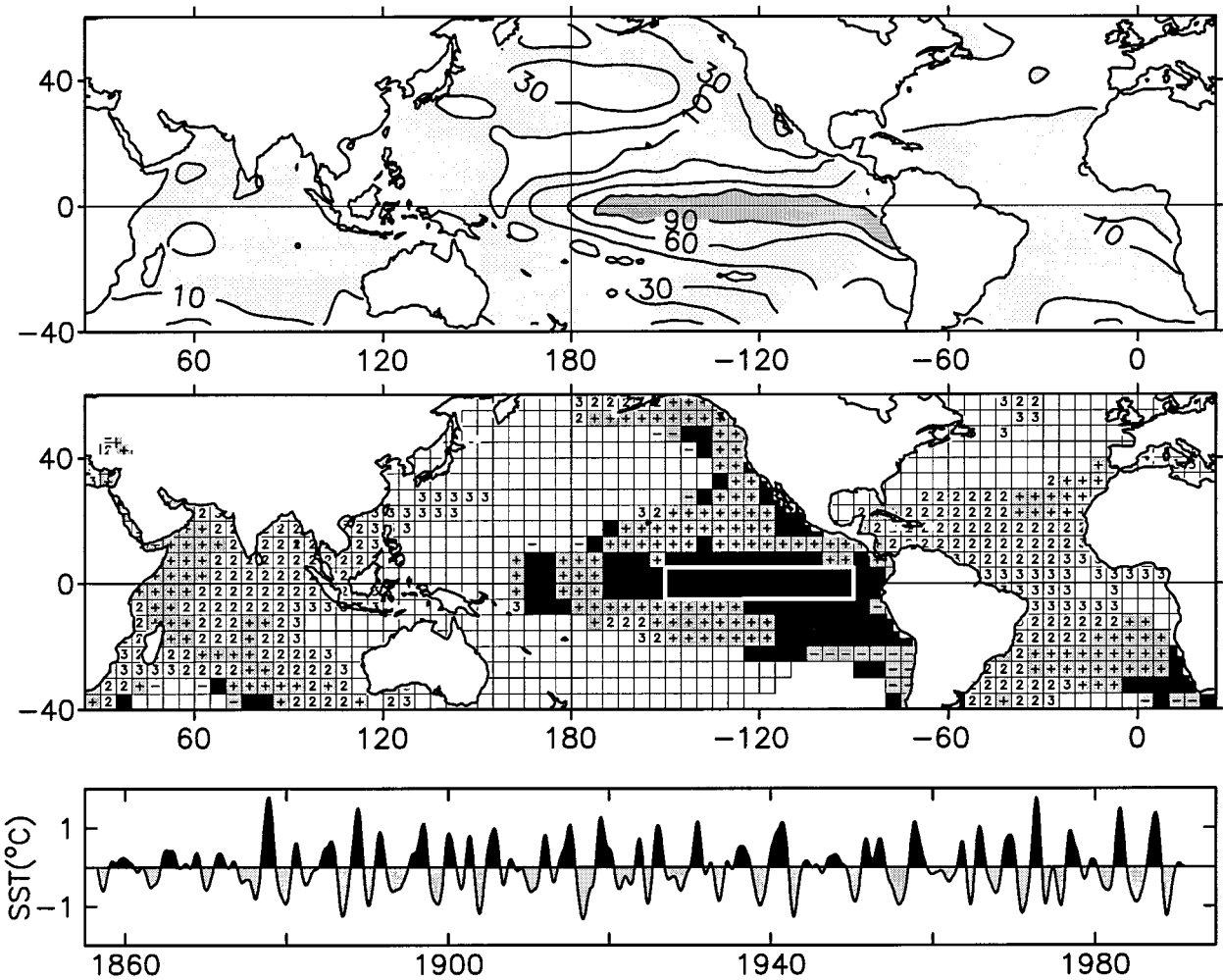
FIG. 2. First CEOF, describing the global ENSO variability. (upper) Spatial distribution of the amplitude with respect to the modal reconstruction over the NINO3 index region (white rectangle, middle panel). Contours shown are 10, 30, 60, and 90. A score of 100 is the average amplitude over the NINO3 region. (middle) Spatial distribution of phase lag (seasons); $+/-$ indicates that the data lags/leads NINO3 (lower panel) by one season and positive numbers indicate data lags of more than one season. Unfilled squares have approximately opposite phase ($180° \pm 40°$) or insignificant amplitude (<10). (lower) Temporal reconstruction of the mode-related variability averaged over the NINO3 index region.

tor. Regions of maximum amplitude occur near $\pm15°$–$20°$ with a two-season lag, consistent with the results of Enfield and Mayer (1997). The Indian Ocean is similarly lagged through eastward phase propagation, consistent with Latif and Barnett (1995). Very little coherent variability is found in the North Atlantic, north of $20°$–$30°N$. The lack of coherent variability off Angola ($0°$–$20°S$) and the somewhat larger lags in the western equatorial Atlantic are qualitatively consistent with the structures found by Enfield and Mayer (1997).

The above characteristics of the global ENSO are consistent with the similar but more detailed analysis of Lanzante (1996). Although Lanzante does not discuss this, his breakdown of the 1875–1979 data period into three shorter periods shows that the larger lags in the equatorial Atlantic existed only during 1950–79 and not

during the previous 75 yr. His tropical Atlantic lags are quite uniform during the earlier periods and similar to the modern lags in the $5°$–$15°N$ band (Enfield and Mayer 1997; Fig. 2, middle panel). It is not clear whether the meridional lag structure in the Atlantic is a nonrobust feature of the system or one that is more ubiquitous but poorly captured under the sparser sampling of the earlier periods.

4. Ordinary versus complex EOFs

To form a "non-ENSO" global dataset, the global SSTA reconstruction from the leading CEOF mode in the ENSO band (Fig. 2) is subtracted from the low-passed (1.5 yr) K98 data. We then remove a linear trend at every grid point (Fig. 1). Both ordinary EOF and

TABLE 1. Each row corresponds to the global ENSO or one of the three leading modes of non-ENSO variability, as indicated by the first column. The last four columns show the percentages of grid points where the magnitude of the zero lag correlation of the local CEOF temporal realization with the EOF expansion coefficients exceeds the value indicated by the header. Only grid points where the spatial amplitude exceeds 0.02 are considered; the percentage of total grid points considered is shown in the second column.

Mode	% >0.02	>0.90	>0.80	>0.70	>0.60
ENSO	41.7	4.4	18.5	33.4	50.7
NoE1	51.9	79.7	93.9	95.5	96.0
NoE2	54.4	5.9	80.8	93.0	95.1
NoE3	44.2	0.0	22.5	67.8	90.8

CEOF decompositions are calculated from these residual data. We have opted not to use a complex decomposition of the non-ENSO residuals because the simple EOFs are more straightforward and describe the variability equally as well. The first three EOF modes account for 9%, 8%, and 5% of the total variance in the low-passed K98 data (before ENSO and trend removals). These amounts can be compared with the 17% explained by the ENSO component and the 9% explained by the linear trends (through subtraction).

Why do we contend that complex EOFs are necessary for the global ENSO mode and not for the non-ENSO residuals? Although the need for a complex decomposition of the global ENSO variability is evident from our knowledge of documented lag relationships around the world, other demonstrations of this need can be made. For example, an ordinary EOF decompostition of tropical Pacific SSTA will result in expansion coefficients for the two leading modes that are significantly correlated at lags of several seasons. The lag structure suggests a quadrature relationship, or shared variability that propagates. This did not occur among the leading EOFs of the non-ENSO variability.

Table 1 statistically compares the temporal amplitudes of the ordinary and complex EOF decompositions for the K98 data before (bandpassed, first mode) and after (residuals, three leading modes) removing the global ENSO mode. The temporal reconstruction at each grid point was computed for each of the four CEOF modes, and these were correlated at zero lag with the expansion coefficients for the corresponding ordinary EOF modes. The table summarizes the gridpoint frequency by correlation range where the CEOF spatial amplitude exceeds an approximate threshold for significance, 0.02.

The correlation magnitudes are largest in regions having large spatial amplitude and variability that is in or out of phase with an index region (e.g., the NINO3 rectangular region in Fig. 2). The correlations are lower at grid points where the local CEOF temporal reconstruction significantly lags the index region or the oppositely phased regions. This occurs (a) systematically where true lag relationships exist, as we have described in our discussion of the global ENSO mode in Fig. 2; (b) randomly in regions of very small amplitude, which

we have tried to minimize by not considering the grid points with CEOF amplitudes less than 0.02; and finally (c) even for standing oscillations, in narrow regions of low amplitude and high gradients of spatial phase between areas of in-phase or out-of-phase variability. In the case of b or c, the number of grid points with low correlations increases with mode number because the spatial wavenumber of the variability increases and the spatial amplitudes are broken up into more and smaller regions of large loading.

The Table 1 comparison confirms the need for using the CEOF approach for the global ENSO but not for the non-ENSO variability. As many as 50% of the ENSO mode grid points have correlations smaller than 0.60 and only 4% (19%) have correlations greater than 0.90 (0.80). In contrast, only 4% of the grid points in the leading non-ENSO mode have correlations smaller than 0.60, while 80% (94%) have correlations exceeding 0.90 (0.80). As expected, there is a progressive degradation of the correlations in the next two residual modes. However, even the third mode, which explains only 5% of the total low-passed variance, shows much more correlation than the ENSO mode, which explains 17% of the same variance. Visual comparisons of the spatial distributions confirm that the non-ENSO CEOF modes are very similar to the ordinary EOFs and can be interpreted in the same way.

5. The non-ENSO SST variability

In each of the following sections we describe the corresponding non-ENSO SSTA mode and discuss how it relates to the recent scientific literature on decadal-to-multidecadal climate variability.

a. Mode 1: Pacific interdecadal variability

We show the spatial pattern and temporal reconstruction for the leading non-ENSO EOF mode in Fig. 3. The rectangular box shown in the spatial pattern (upper panel) is a region of large spatial amplitude that references the temporal amplitudes (°C, lower panel). The spatial pattern is mapped as regression coefficients of the data with respect to the temporal reconstruction for the reference rectangle (lower panel) and hence is a gain map in the same sense as Fig. 2 (upper panel). The heavy dashed lines in the central North Pacific indicate the positions of the subtropical front (STF) and the subarctic front (SAF) as referred to by Nakamura et al. (1997) and discussed later in this paper.

The highest Pacific spatial loadings are found over three main regions: negative loadings over a zonal band of the central and western North Pacific centered near 35°N, positive loadings over alongshore swaths off the coasts of North and South America, and in positive oceanic lobes north and south of the equator between 100° and 140°W. Secondary regions of positive loadings
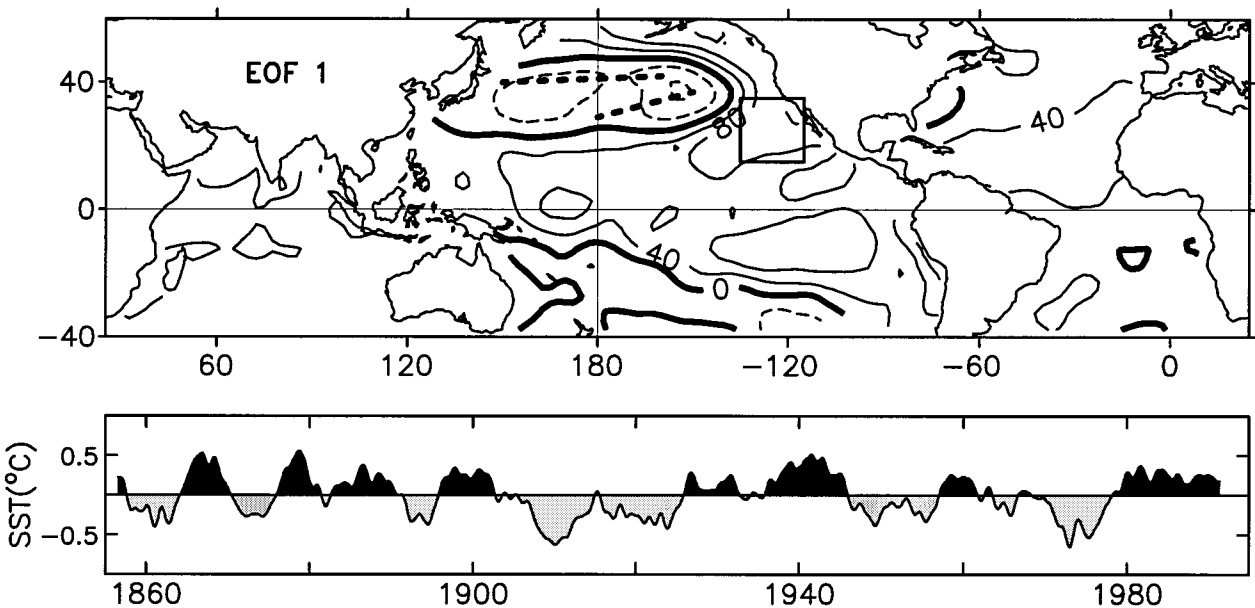
FIG. 3. First EOF of the non-ENSO residual dataset, describing the Pacific interdecadal variability. (upper) Spatial distribution of the response with respect to the modal reconstruction over the index region (rectangle); contour interval is 40 and dashed contours are negative. A score of 100 is the average response over the index region. The heavy dashed lines in the central North Pacific indicate the positions of the STF and the SAF as referred to by Nakamura et al. (1997). (lower) Temporal reconstruction of the mode-related variability averaged over the index region.

are found in the tropical North Atlantic and northern Indian Oceans.

The mode 1 spatial pattern in the Pacific corresponds closely to that documented by a number of investigators in reference to Pacific interdecadal variability, sometimes referred to as the Pacific Decadal Oscillation (PDO). This pattern can be seen in the work of Latif and Barnett (1994), Trenberth and Hurrel (1994), Deser et al. (1996), Latif and Barnett (1996), Mantua et al. (1997), Nakamura et al. (1997), Zhang et al. (1997) and Giese and Carton (1999). Not all analyses show the low-latitude SST lobes, but those of Nakamura et al. (1997) and Zhang et al. (1997) show them well.

Most previous analyses look at variability after 1930 or 1950 and call particular attention to the interdecadal shift that occurred in the late 1970s, which can be seen in the temporal reconstruction. Figure 3 shows that such shifts have been occurring consistently throughout the last 140 yr, with alternate regimes that typically last about 10–20 yr at a time. The temporal variations look like a detrended version of the global warming mode documented by Enfield and Mestas-Nuñez (1999), which emerged as the first CEOF of the residual K98 data but without prior detrending. That these two very different timescales (secular and interdecadal) should project onto the same multivariate mode (i.e., as shown by Enfield and Mestas-Nuñez) is consistent with the similarity in their spatial distributions (Figs. 1 and 3). This raises the interesting possibility that the two timescales share a similar mechanism that could therefore explain how the global warming signal is distributed

around the World Ocean. It also provides compelling evidence for, and explanation of, the fact that global warming in the twentieth century has undergone a series of apparent pauses and accelerations (Houghton et al. 1996).

Any successful hypothesis as to how the Pacific interdecadal mode of variability arises must explain the spatial pattern, the strength and persistence of the negative loading feature in the North Pacific, the long time-scale, and how the shifts between alternate states occur. Scientists have made many suggestions in recent years as to what the PDO mechanism(s) may be but the issue remains unresolved.

There exists fair agreement that the central North Pacific SST changes (negative loadings in Fig. 3) result from a combination of zonal wind-induced surface fluxes, dominated by the latent heat process (e.g., Cayan 1992), and meridional temperature advection by anomalous Ekman transports (Miller et al. 1994). During the North Pacific cooling phase when the westerlies are more energetic, the meridional SST gradient becomes accentuated in the latitude band centered near 30°N, which strengthens the mid-Pacific subtropical jet and further intensifies the surface westerlies. This results in a positive feedback in the direction of cooler temperatures and persistence of the cool anomaly.

During the early part of the North Pacific cool phase, the midlatitudes experience anomalous cyclonic circulation and strengthened westerlies in a region overlying the cool anomaly, while the trade winds weaken over the low latitudes of the central and western Pacific
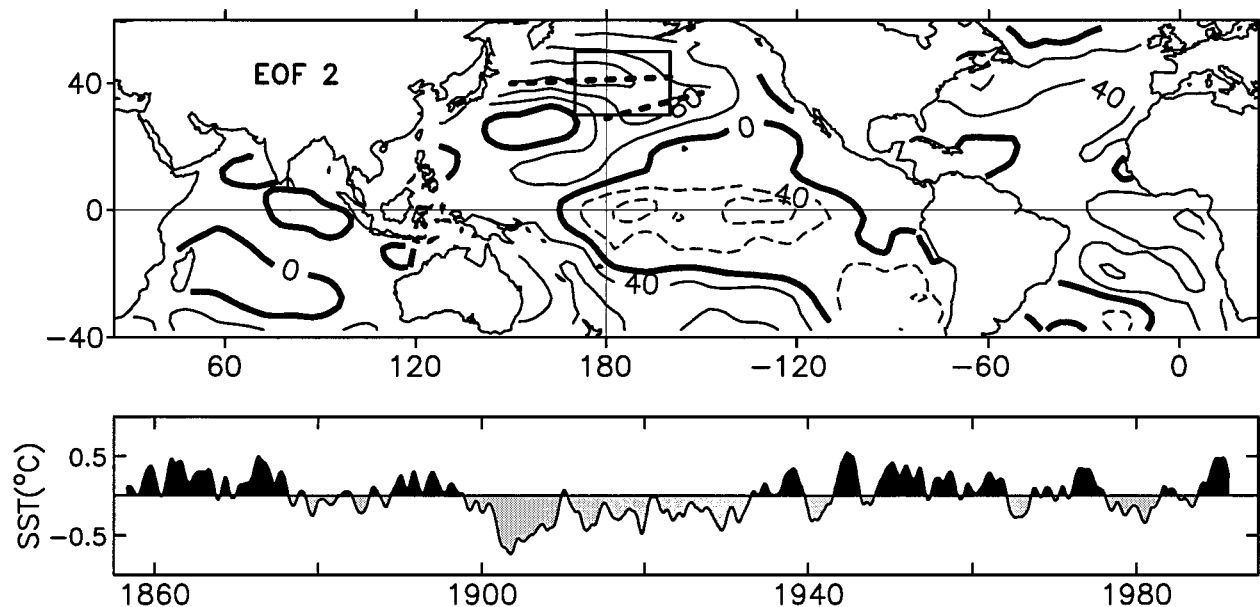
FIG. 4. As in Fig. 3; second EOF of the non-ENSO residual dataset, describing the Pacific multidecadal variability.

(Giese and Carton 1999). According to Giese and Carton (1999) the latter feature is consistent with an equatorward shift of the atmospheric circulation at this time. Just as occurs during the warm phase of ENSO, the shift to weakened trades induces warming over a wide swath of the central and eastern tropical Pacific through basin-scale readjustment via Kelvin and Rossby waves.

We speculate that the arcuate pattern of low-latitude warming and its extensions to high latitudes along the coasts of North and South America (Fig. 3) are characteristic of the ocean basin readjustment process that results from the weakened trade wind regime. The resulting relaxation in the circulation is accommodated by a deepening of the thermocline in the east and in the equatorward limbs of the subtropical gyres. Where the thermocline is normally shallow, that is, along the midlatitude coasts and the zonal thermocline ridges near $\pm 10°$, the deepening leads to reduced mixed layer entrainment of colder water from below and a maximum of surface warming. One also expects a slackening of the equatorward advection of cooler extratropical water. Consistent with this, Giese and Carton (1999) show an associated EOF of heat content with lobes of maximum loading near $\pm 10°$, and a pattern very similar to Fig. 3, in general. They show a relative minimum of interdecadal variability on the equator itself, also similar to Fig. 3.

For most of the 1980s and early 1990s, the Pacific has been in such a northern cold (tropical warm) phase. If we adopt the ENSO paradigm as a useful analog for producing an oscillation, a negative feedback is required to move the PDO into a North Pacific warm phase, while an appropriate delay mechanism is needed to produce the interdecadal timescale between reversals. One proposal is that the wind-forced SST cooling over the central North Pacific subducts and migrates equatorward from midlatitudes along the density surfaces of the main thermocline. The most compelling evidence for this comes from subsurface thermal observations of the shift in the late 1970s wherein the prior North Pacific warm anomaly was observed to subduct and advect to low latitudes along the tropical thermocline (Deser et al. 1996; Zhang et al. 1998). A coupled model simulation by Gu and Philander (1997) also reproduces this kind of behavior. They suggest that the migration may reach as far as the eastern equatorial Pacific where the anomalies can be upwelled within the cold tongue and can subsequently feed back on the North Pacific through a corresponding change in the westerlies, thus causing the sign of the oscillation to change.

Deser et al. (1996) only follow the warm anomaly of the 1960s equatorward as far as 20°N, the southern limit of their data domain. In their model simulation, Lysne et al. (1997) see an equatorward migration of the warm temperature anomaly to 10°N, consistent with Deser et al. However, they see a parallel and somewhat quicker warming on the equator, which they suggest arrives from the central North Pacific through wave dynamics via the western ocean boundary. They trace the anomaly back to the central North Pacific but its ultimate origin is unknown. Either or both of these mechanisms (subduction/advection or Rossby/Kelvin waves) could provide the delay and effect a reversal of conditions at low latitudes.

b. Mode 2: Pacific multidecadal variability

The second mode spatial pattern (Fig. 4) shows some similarities to that of the first mode. A zonal band of

highest loadings extends westward from 160°W along 45°N, while moderately high loadings of opposite sign extend along a ±15° swath of the central equatorial Pacific, with a somewhat weaker extension to the southeast, west of Chile. In most other respects, however, the distribution differs from its first mode counterpart. The high amplitudes along the west coast of North America are missing and the low-latitude variability is centered on the equator rather than ±10°–15°. Moreover, there is no manifestation in the Indian Ocean and the significant Atlantic variability (in phase) is limited to two regions where the first mode is unimportant: in a zonal band along 40°–45°N and in the tropical southeast Atlantic. The greatest difference, however, is that the temporal variability (lower panel) is dominated by longer, multidecadal oscillations.

Aside from the differences noted above, the possibility that the second mode contains a significant quadrature component of the first mode variability seems unlikely. Had that been the case, we do not think the EOF and CEOF versions of the mode would have corresponded so closely (section 4). There is a greater than 95% significant cross correlation (0.38) between the modes with first-mode coolings lagging second-mode warmings by 6 yr in the North Pacific, implying an appropriate 2–3 decade periodicity for a propagating oscillation. However, mode 1 coolings also precede mode 2 warmings with 95% significance (0.29) at a lead time of 8 yr, whereas a quadrature relationship similar to a principal oscillation pattern would predict mode 1 warmings leading mode 2 warmings. We do not attribute great significance to the cross correlations because little of the variance in one mode is explained by the other (10%–15%) and the timescales of the implied relationships may not be well resolved by the length of the time series.

Prior results regarding mode 2 are scarce and best exemplified by the study of Nakamura et al. (1997), who performed an EOF decomposition on SSTA for a rectangular region of the central North Pacific, 1951–92 (periodicities of 7 yr or less removed). Although their spatial and temporal domains are very different from ours, they essentially reproduce the modal variability seen in our first two non-ENSO modes, but in reverse order. Their first mode (corresponding to our Fig. 4) shows a region of intense SSTA variability along 42°N, coinciding with the SAF north of the Kuroshio extension. Their second mode (corresponding to our Fig. 3) extracts strong variability farther east and south of 45°N, coinciding with the STF north of Hawaii. The temporal variabilities are essentially those of Figs. 4 and 3, respectively, for the period after 1950. In their search for associations outside the EOF domain, Nakamura et al. (1997) did not encounter in their SAF mode the strong antinode that we find on the equator in Fig. 4, but they had strong anticorrelation in the Gulf of Alaska. We attribute these differences to the much larger spatial and temporal domains of our analysis. Low-latitude anti-

correlation does occur in their STF mode (as in Fig. 3). They use the anticorrelation (STF) or noncorrelation (SAF) as an indication of mode forcing by tropical SSTA and conclude that the SAF mode is essentially maintained only by midlatitude interactions. Our results (modes 1, 2) are consistent with the STF and SAF frontal locations in Nakamura et al. (1997). However, taken over more than a century of data, the SAF mode (Fig. 4) has a more multidecadal timescale than for just the 1951–92 period. The fact that we see a strong equatorial anticorrelation in that mode suggests that it may not be only a midlatitude process.

Although mode 1 corresponds very well to most other analyses of Pacific interdecadal variability, there are enough differences between those analyses in terms of methods, period of analysis, and the details of the resulting spatial distributions that some of the mode 2 variability may be present in some of them and not in others. Using a method very similar to ours, Zhang et al. (1997) produce temporal variability for the period 1950–93 that is strikingly similar to that of Fig. 3 (lower panel) and a spatial pattern showing all the features of Fig. 3 (upper panel), including the tropical sidelobes near ±10°. We contend that such analyses isolate Pacific interdecadal variability similar to our first non-ENSO mode (Fig. 3). However, an analysis based on the correlation of air temperatures with a North Pacific pressure index does not show the off-equatorial lobes (Trenberth and Hurrell 1994). Nor do the sidelobes appear in a pan-Pacific regression of SSTA on a PDO component of an EOF analysis done only for North Pacific SSTA (Mantua et al. 1997). Comparison of the Mantua et al. (1997) PDO index with the mode 1 time history (Fig. 3, lower panel) or with Zhang et al. (1997) shows discrepancies that are consistent with the inclusion of the mode 2 warming trend (1905–50) in the Mantua et al. index. Hence, the mode 2 variability may be included with mode 1 variability in some analyses that have addressed the Pacific interdecadal mode. Because the temporal variabilities of the two modes are so different, they should probably be treated separately.

c. Mode 3: Atlantic multidecadal variability

The third non-ENSO mode has its highest spatial loadings in the high latitudes of the North Atlantic, immediately south of Greenland (Fig. 5). Intensities of secondary magnitude (decreasing order of intensity) are found in the eastern equatorial Pacific, the Pacific north of 40°N, the tropical South Atlantic, and the Indian Ocean. This is the only one of the three non-ENSO modes to display a meridionally antisymmetric pattern in the tropical Atlantic, spanning the intertropical convergence zone.

Finding regions of moderate loading in other oceans, especially the Pacific, raises the suspicion that the mode may not be robust under rotation; that is, one or more secondary regions may not be well associated with the
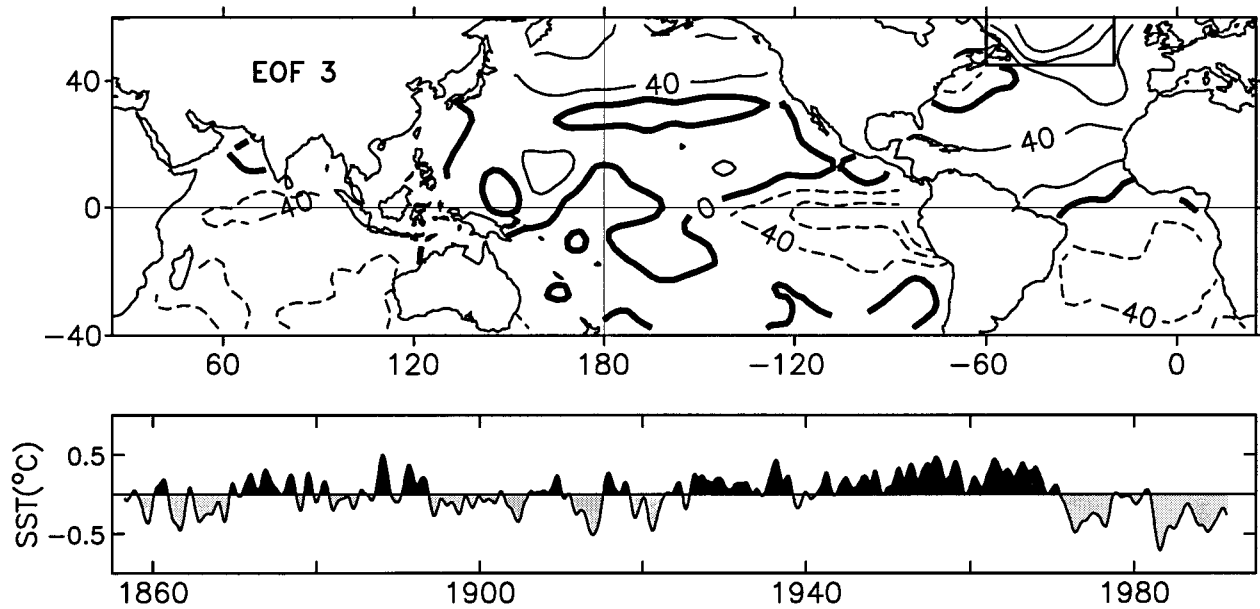
FIG. 5. As in Fig. 3; third EOF of the non-ENSO residual dataset, describing the Atlantic multidecadal variability.

mode. To test this we performed a varimax rotation of the modes. The rotation (not shown) separates the eastern Pacific and tropical South Atlantic features into modes temporally distinct from a third mode having the (unrotated) mode 3 spatial pattern north of the ITCZ in the Atlantic. The rotated mode for the North Atlantic retains the multidecadal temporal character of Fig. 5, and the loadings in the tropical North Atlantic and the Gulf of Alaska increase considerably. The eastern Pacific variability rotates into Pacific patterns that share similarities with Figs. 3 and 4 and have both decadal and multidecadal variability. Under rotation, the South Atlantic becomes primarily a mixture of interannual and decadal variability but with a subtle multidecadal modulation similar to Fig. 5. It is consistent with the most energetic components of variability found in analyses of the South Atlantic only (Venegas et al. 1996, 1997). The question of how one should think of the eastern Pacific variability or whether an Atlantic dipole actually exists as a dynamical system will be subjects of papers in preparation that deal with the rotated modes. The point for this paper is that the unrotated third mode (Fig. 5) is most characteristically a North Atlantic multidecadal mode involving both the tropical North Atlantic and the region south of Greenland, plus the high-latitude North Pacific. It, and the North Atlantic, are the focus of the discussion that follows.

A salient feature of the temporal reconstruction (Fig. 5) is the superposition of two very different timescales: interannual and multidecadal. That these fall out in the same mode suggests that they have similar spatial loadings. The analyses of Delworth et al. (1993) and Delworth (1996) indeed show a similar, zonally banded structure for both but with a more elongated and pro-

nounced antinode east of the continental United States. Bjerknes (1964) distinguished these timescales, proposing that ocean processes drive the longer while atmospheric forcing of SSTA through surface fluxes drives the shorter. The modeling work of Delworth et al. (1993) and Delworth (1996) supports this idea.

More than a century of instrumental data has documented the slow variability of North Atlantic SSTA (Deser and Blackmon 1993; Kawamura 1994; Kushnir 1994; Hansen and Bezdek 1996; Halliwell 1997; etc.). Tree-ring research has confirmed the 30–80-yr periodicity in air temperatures over longer intervals (D'Arrigo et al. 1996). At its most basic level, the variability can be understood as the switching of a zonally banded North Atlantic SSTA pattern (similar to Fig. 5) at intervals of 15–40 yr. The atmospheric links to the SSTA variability occur in the context of the North Atlantic Oscillation (NAO) in tropospheric pressure fields. The NAO is associated with slow fluctuations in the midlatitude westerlies of the North Atlantic and in storm tracks over Europe (e.g., Deser and Blackmon 1993; Kushnir 1994; Hurrell 1995). The best-documented phase change occurred in the late 1960s when SST over the region south of Greenland went from warm to cool. Simultaneously the NAO went into its positive (high index) phase, the westerlies accelerated, and storm tracks shifted northward into Scandinavia leaving southern Europe with a more benign climate (e.g., Hurrell 1995). A more recent reversal to the opposite phase may have occurred in the 1995/96 winter (Kerr 1997).

The NAO-related ocean changes may not happen solely as a stationary oscillation. Recent research suggests that slow propagations may be involved in both SSTA (Hansen and Bezdek 1996) and in sea level pres-

sure (Halliwell 1997). However, our modal analyses detected no SSTA progression, even with the CEOFs. This may be due to the coarse global resolution (5°×5°) used here.

Proposed mechanisms for the persistence and switching of the SSTA pattern and the NAO mainly involve the thermohaline circulation of the Atlantic (Bjerknes 1964; Delworth et al. 1993; Curry et al. 1998; Delworth et al. 1997). One mechanism is based on changes in the winter subduction of surface water to deeper levels in the Labrador Sea, controlled by SST anomalies advected around the North Atlantic (Curry et al. 1998). In another proposal the subduction changes are related to fluctuations of the East Greenland Current, the sea ice and freshwater it transports from the Arctic, and the consequent changes of salinity in the Labrador Sea (Delworth et al. 1997). The advective changes in both cases involve feedback with the NAO and its associated North Atlantic wind patterns.

6. Tropospheric associations in winter

The distributions of December–February (DJF) geopotential height for the 500-hPa pressure level, associated with the three non-ENSO modes, are shown in Figs. 6, 7, and 8. These are composite maps on a polar stereographic projection of the Northern Hemisphere. Each map is formed by first averaging separately the maps for all DJF months where the corresponding modal reconstruction of SSTA (Figs. 3, 4, and 5, bottom panels) exceeds 0.05°C (positive composite) or is less than −0.05°C (negative composite), respectively. Each of the final maps is half of the difference between the positive and negative composites for that SSTA mode. The implication of quasi linearity in the relationships shown is valid because the positive and negative composites are similar but oppositely phased patterns. The summer composites (not shown) are very weak and poorly defined compared with the winter patterns. Consistent with this, the patterns for all seasons combined (not shown) are weaker versions of the winter patterns.

The three associated winter patterns will be discussed as to how they compare with the teleconnection patterns found in the classification scheme of Barnston and Livezey (1987), based on 700-hPa heights. Although the geopotential levels are different, the patterns typically maintain their character between levels, as can be seen by comparing the Barnston and Livezey (1987) compilation with those of Wallace and Gutzler (1981).

The 500-hPa pattern associated with non-ENSO mode 1 (Fig. 6) appears most similar to the Pacific–North American (PNA) pattern of Barnston and Livezey. This is not surprising because the ENSO SSTA distribution excites the PNA pattern, while the non-ENSO mode 1 distribution resembles its ENSO counterpart and can therefore be expected to associate similarly with the tropospheric variability. Thus, when the low-latitude eastern Pacific is warm, we see a deepening of the Aleu-

tian low in the northeastern North Pacific, higher pressure heights over western Canada and Alaska, and lower heights over the east coast of North America and as far south as Cuba. In the interannual PNA, however, the departures near the southeastern United States are more intense (using the Aleutian low as a reference) than is the case in Fig. 6.

Figure 7, corresponding to non-ENSO mode 2, appears most similar to the North Pacific (NP) pattern of Barnston and Livezey (1987). In both cases, there are two elongated zonal lobes of the same polarity spanning regions on opposite sides of the North Pole. One lobe stretches from east Asia to the Gulf of Alaska, and the other covers Europe and much of the North Atlantic. Between them is an antinodal region roughly concentric with the polar vortex, with an equatorward dip into western North America, also as seen in the NP pattern. However, in the Barnston and Livezey classification the lobe in the North Pacific is the most zonally extensive, whereas for the non-ENSO case shown here the most zonally extensive feature is on the Atlantic side. In addition, the NP pattern is most characteristic of the late spring and early summer, and not of the winter season. In the Atlantic sector, the pattern of Fig. 7 is also very similar to those frequently encountered with the NAO. However, the strong lobe in the Aleutian low region is missing from the NAO patterns.

Since both ENSO and mode 2 have significant SSTA loadings in the equatorial Pacific, we might inquire if the 500-hPa association with mode 2 (Fig. 7), in the region of the Aleutian low, is consistent with the PNA signature for the Aleutian low. For this to be so, negative height departures should correspond to warm SSTs on the equator. In Fig. 7 positive 500-hPa departures in the eastern North Pacific correspond to negative loadings in the equatorial portion of the SSTA pattern for mode 2; hence, the relationship indeed holds. We note, however, that the positive 500-hPa departures west of California are somewhat south of the Aleutian low and of the corresponding negative PNA-like feature in Fig. 6.

The mode 3 SSTA pattern (Fig. 5) has a 500-hPa composite (Fig. 8) that strongly resembles the NAO pattern in the Barnston and Livezey classification, but has some differences as well. The pattern is strongest over western Greenland where the NAO is also strong during winter months. Secondary centers of the same sign occur over the tropical North Atlantic and in the North Pacific over the outer Aleutian Islands. The main antinode is an elongated zone of negative departures stretching from eastern North America (where it is weaker) to central Europe (where it is stronger). The negative departures are comparatively weak, however, when compared with the corresponding antinode in the region of the Bermuda–Azores high, as found in the Barnston and Livezey classification. The tropical North Atlantic feature west of northwest Africa is stronger than in the classification, where it is well defined only during some summer months. The relationship with SSTA is
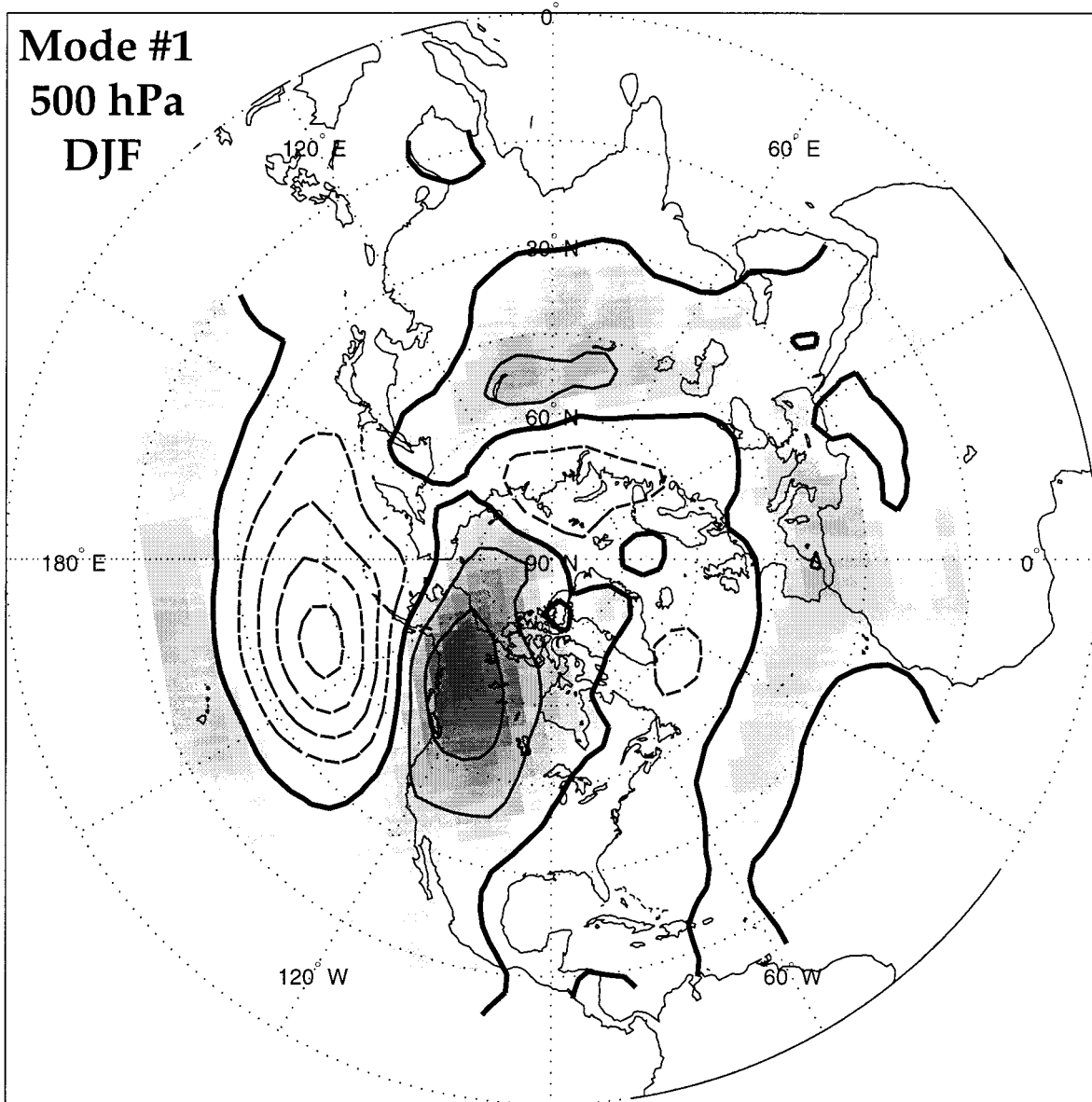
FIG. 6. Half the difference between composite averages of 500-hPa pressure heights with respect to positive and negative values of the mode 1 temporal reconstruction of Fig. 3, as explained in the text. Contour interval is 20 geopotential meters, positive (negative) contours are solid (dashed), and the bold contour is zero. Positive values are shaded.

such that when the North Atlantic is warm (Fig. 5), the Icelandic low is weaker and the westerly winds across the North Atlantic into Europe are also weaker. This corresponds to the negative phase of the NAO and is consistent with the SSTA–NAO relationships observed by others (e.g., Curry et al. 1998).

The most glaring discrepancy with the Barnston and Livezey classification is that the Aleutian node (Fig. 8) does not appear in the NAO pattern. Where this feature does appear is in the Arctic Oscillation (AO) pattern of Thompson and Wallace (1998), which they find to be similar to the NAO in most other respects. Most of the other

aspects of Fig. 8, discussed above, also appear in the AO pattern. The main discrepancy with the AO is that the node over southern Greenland does not take a form consistent with the polar vortex shown by Thompson and Wallace (1998), which includes the North Pole but is skewed into the Greenland sector. Overall, however, we find the pattern more similar to the AO than to the NAO.

7. Discussion

We wish to note that our method of defining a global ENSO mode assumes that ENSO variability is limited
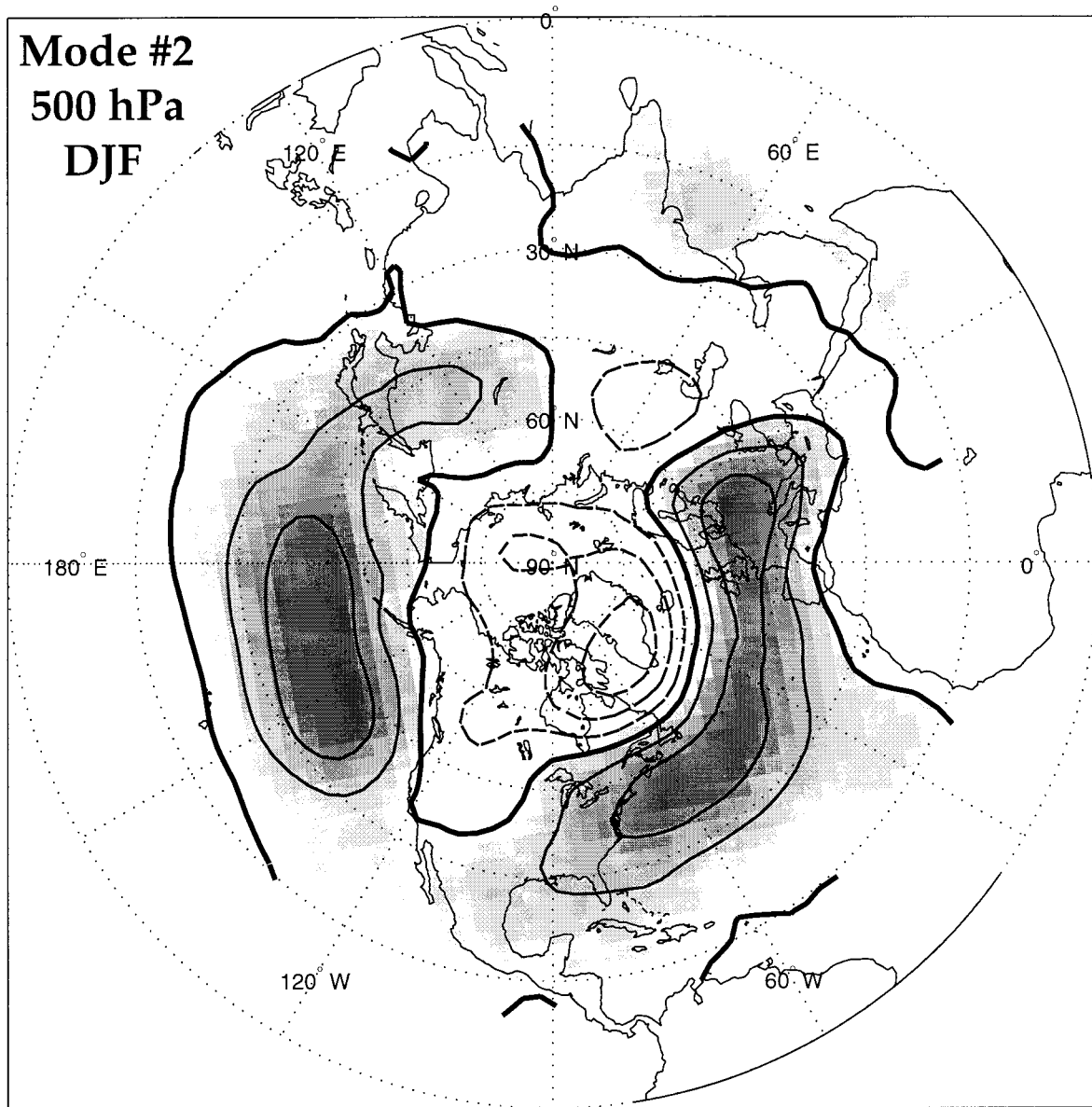
FIG. 7. As in Fig. 6 but with respect to the temporal reconstruction of mode 2 (Fig. 4).

to a band with periods of less than 8–10 yr. In calculating the global ENSO mode we bandpassed our data because we felt that the complex EOF method (Hilbert transform) would be most effective if not applied to a wide spectrum of variability. Although we are unaware of any claim that ENSO includes variability at lower frequencies, it is certainly possible that nonstationarities exist, that is, that the interannual ENSO statistics themselves are time variant on longer timescales. The global ENSO mode should capture changes in event intervals or amplitudes as long as the spatial distribution of anomalies remains essentially unchanged. We also note that the non-ENSO modes do contain significant interannual variability, especially modes 2 and 3. By our definition

of the global ENSO this interannual variability is presumed to be non-ENSO in nature. However, it could contain certain fluctuations that on closer inspection might be unusual ENSO anomalies that do not fit with the canonical pattern captured by the global ENSO mode. Nevertheless, while the ENSO extraction may not be perfect, it certainly accounts for the principal SSTA features known to exist in ENSO variability.

Neither do we claim that the non-ENSO modes are perfect representations of the decadal-to-multidecadal climate variability. A varimax rotation of the residual EOFs (research in progress) suggests that the eastern equatorial Pacific antinode in Fig. 5 may not be an oceanic extension of NAO-related Atlantic variability. The
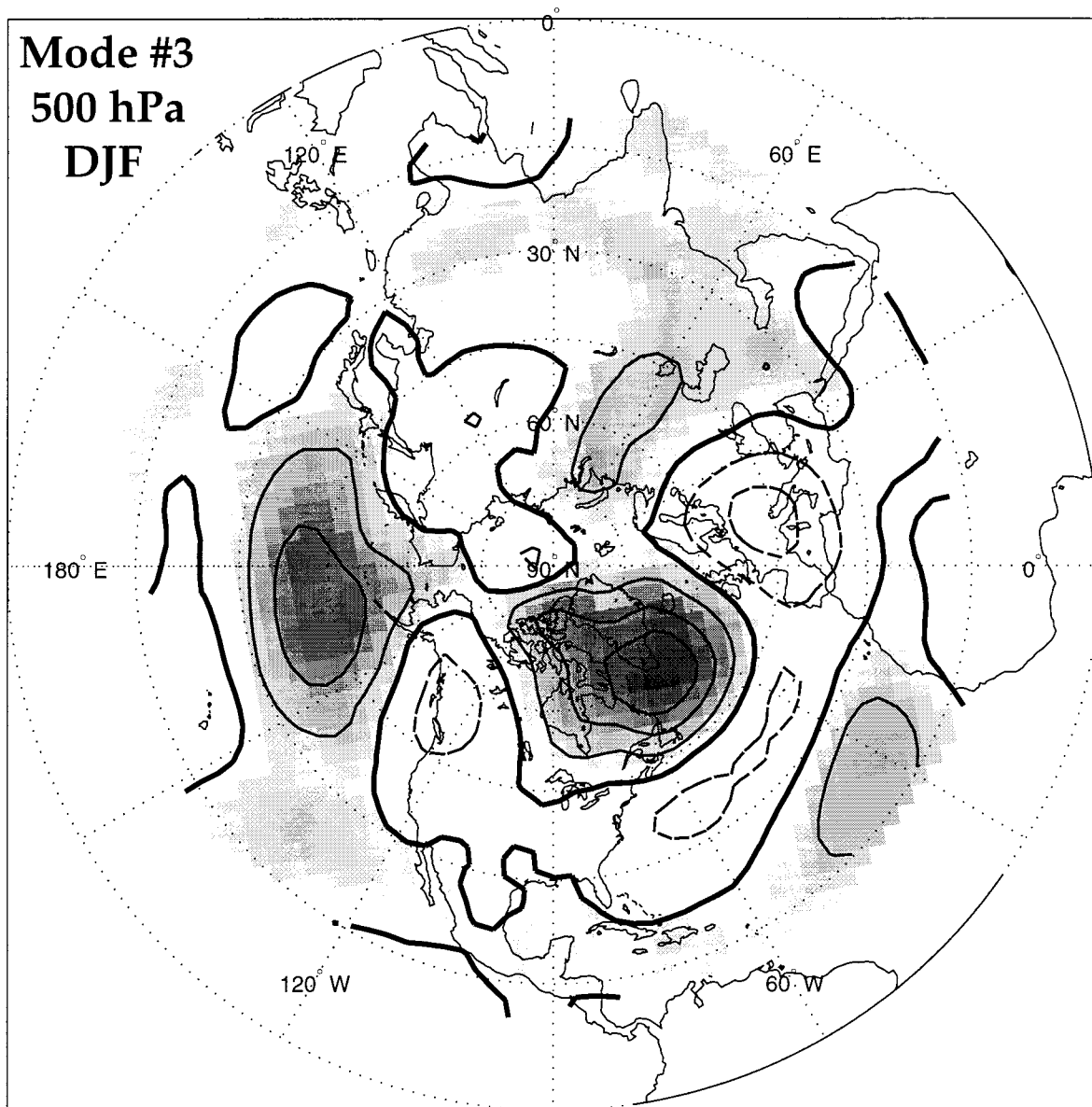
FIG. 8. As in Fig. 6 but with respect to the temporal reconstruction of mode 3 (Fig. 5).

rotated analysis also reveals that the South Atlantic variability is much more interannual in character while the entire North Atlantic retains the multidecadal signature seen in Fig. 5. This is interesting because it suggests that the whole question of a dynamically linked tropical dipole oscillation needs to be carefully revisited by future research. In the context of this paper it means that the AO–NAO associations suggested by Fig. 8 must be considered more in connection with the North Atlantic SSTA than with the South Atlantic.

The interesting observation of Nakamura et al. (1997) that modal variabilities in the central North Pacific tend to line up either with the SAF or the STF should be carefully examined. As noted earlier, the loadings in the North Pacific for mode 1 (Fig. 3) resemble the second EOF (STF) of Nakamura et al. (1997) while in mode 2 (Fig. 4) they resemble more their first EOF (SAF). However, neither of our modes coincides with the SAF location as well as their first EOF and both have large amplitude loadings near the STF location. The discrepancies between the two analyses can probably be ascribed to the much different spatial and temporal domains of the decompositions.

An obvious implication of the Pacific frontal relationships of Nakamura et al. (1997) is that the winter subduction of temperature anomalies within these regions may be involved in oscillation mechanisms for the modes, in a manner similar to that suggested by Gu

and Philander (1997) and Zhang et al. (1998). The Gu and Philander model trajectories for subducted water that can later upwell at low latitudes start near to, but slightly south of, the STF location and are possibly consistent with an STF subduction mechanism for both mode 1 and mode 2. However, the trajectories are far from the SAF location and it is probable that water subducted at the SAF never gets to low latitudes. Finally, we note that the modal variabilities seen by Nakamura et al. (1997) at the frontal locations may be due more to meridional migrations of the fronts than to fluctuations in SST at the location of maximum gradient (convergence).

The strong loadings of SSTA in the Gulf of Alaska on the third non-ENSO mode (Fig. 5) are an interesting feature of this analysis. This two-ocean expression of AO–NAO-related variability survives under a varimax rotation (work in progress), confirming that the Gulf of Alaska variability has a true AO–NAO character. We earlier pointed out that the North Pacific node in the 500-hPa pattern of Fig. 8 is not found in the classified patterns for the NAO (Barnston and Livezey 1987) and is more consistent with the AO oscillation of Thompson and Wallace (1998). That node, in conjunction with anticorrelated 500-hPa variability over western Canada, implies anomalous southwesterly flow off the west coast of North America, poleward into the Gulf of Alaska. Although the 500-hPa winds cannot be related directly to local SSTA, they are at least qualitatively consistent with the kind of surface wind conditions that can produce warming in the northern Gulf of Alaska. Moreover, the analysis of Thompson and Wallace (1998) shows that the North Pacific node of the AO is present throughout the lower troposphere. This would explain why the third non-ENSO mode of SSTA (Fig. 5) has a strong expression in that region as well as in the North Atlantic.

REFERENCES

Barnston, A. G., and R. E. Livezey, 1987: Classification, seasonality, and persistence of low-frequency atmospheric circulation patterns. *Mon. Wea. Rev.,* **115,** 1083–1126.

——, and Coauthors, 1994: Long-lead seasonal forecasts—Where do we stand? *Bull. Amer. Meteor. Soc.,* **75,** 2097–2114.

Bjerknes, J., 1964: Atlantic air–sea interaction. *Advances in Geophysics,* Vol. 10, Academic Press, 1–82.

Cane, M. M., A. C. Clement, A. Kaplan, Y. Kushnir, D. Pozdnyakov, R. Seager, S. E. Zebiak, and R. Murtugudde, 1997: Twentieth-century sea surface temperature trends. *Science,* **275,** 957–960.

Cayan, D. R., 1992: Latent and sensible heat flux anomalies over the northern oceans: The connection to monthly atmospheric circulation. *J. Climate,* **5,** 354–369.

Covey, D. C., and S. Hastenrath, 1978: The Pacific El Niño phenomenon and the Atlantic circulation. *Mon. Wea. Rev.,* **106,** 1280–1287.

Curry, R. G., M. S. McCartney, and T. M. Joyce, 1998: Oceanic transport of subpolar climate signals to mid-depth subtropical waters. *Nature,* **391,** 575–577.

D'Arrigo, R. D., E. R. Cook, and G. C. Jacoby, 1996: Annual to decadal-scale variations in northwest Atlantic sector temperatures inferrred from tree rings. *Can. J. For. Res.,* **26,** 143–148.

Delworth, T. L., 1996: North Atlantic interannual variability in a coupled ocean–atmosphere model. *J. Climate,* **9,** 2356–2375.

——, S. Manabe, and R. J. Stouffer, 1993: Interdecadal variations of the thermohaline circulation in a coupled ocean–atmosphere model. *J. Climate,* **6,** 1993–2011.

——, ——, and ——, 1997: Multidecadal climate variability in the Greenland Sea and surrounding regions: A coupled model simulation. *Geophys. Res. Lett.,* **24,** 257–260.

Deser, C., and M. L. Blackmon, 1993: Surface climate variations over the North Atlantic Ocean during winter: 1900–1989. *J. Climate,* **6,** 1743–1753.

——, M. A. Alexander, and M. S. Timlin, 1996: Upper-ocean thermal variations in the North Pacific during 1970–1991. *J. Climate,* **9,** 1840–1854.

Enfield, D. B., and D. A. Mayer, 1997: Tropical Atlantic SST variability and its relation to El Niño–Southern Oscillation. *J. Geophys. Res.,* **102,** 929–945.

——, and A. M. Mestas-Nuñez, 1999: Global modes of ENSO and non-ENSO SST variability and their associations with climate. *El Niño and the Southern Oscillation: Multiscale Variability and Its Impacts on Natural Ecosystems and Society,* H. F. Diaz and V. Markgraf, Eds., Cambridge University Press, in press.

Giese, B. S., and J. A. Carton, 1999: Interannual and decadal variability in the tropical and midlatitude Pacific Ocean. *J. Climate,* in press.

Gu, D., and S. G. H. Philander, 1997: Interdecadal climate fluctuations that depend on exchanges between the tropics and extratropics. *Science,* **275,** 721–892.

Halliwell, G. R., Jr., 1997: Decadal and multidecadal North Atlantic SST anomalies driven by standing and propagating basin-scale atmospheric anomalies. *J. Climate,* **10,** 2405–2411.

Hansen, D. V., and H. F. Bezdek, 1996: On the nature of decadal anomalies in North Atlantic sea surface temperature. *J. Geophys. Res.,* **101,** 8749–8758.

Hastenrath, S., L. C. de Castro, and P. Aceituno, 1987: The Southern Oscillation in the Atlantic sector. *Contrib. Atmos. Phys.,* **60,** 447–463.

Houghton, J. T., L. G. Meira Filho, B. A. Callander, N. Harris, A. Kattenberg, and K. Maskell, Eds., 1996: *Climate Change 1995: The Science of Climate Change.* Cambridge University Press.

Hurrell, J. W., 1995: Decadal trends in the North Atlantic Oscillation: Regional temperatures and precipitation. *Science,* **269,** 676–679.

Kaplan, A., M. A. Cane, Y. Kushnir, A. C. Clement, M. B. Blumenthal, and B. Rajagopalan, 1998: Analysis of global sea surface temperatures 1856–1991. *J. Geophys. Res.,* **103,** 18 567–18 589.

Kawamura, R., 1994: A rotated analysis of global sea surface temperature variability with interannual and interdecadal scales. *J. Phys. Oceanogr.,* **24,** 707–715.

Kerr, R. A., 1997: A new driver for the Atlantic's moods and Europe's weather? *Science,* **275,** 754–755.

Kushnir, Y., 1994: Interdecadal variations in North Atlantic sea surface temperature and associated atmospheric conditions. *J. Climate,* **7,** 141–157.

Lanzante, J. L., 1996: Lag relationships involving tropical sea surface temperatures. *J. Climate,* **9,** 2568–2578.

Latif, M., and T. P. Barnett, 1994: Causes of decadal climate vari-

ability over the North Pacific and North America. *Science,* **266,** 634–637.

——, and ——, 1995: Interactions of the tropical oceans. *J. Climate,* **8,** 952–964.

——, and ——, 1996: Decadal climate variability over the North Pacific and North America: Dynamics and predictability. *J. Climate,* **9,** 2407–2423.

Lau, N.-C., and M. J. Nath, 1994: A modeling study of the relative roles of tropical and extratropical anomalies in the variability of the global atmosphere–ocean system. *J. Climate,* **7,** 1184–1207.

Lysne, J., P. Chang, and B. Giese, 1997: Impact of the extratropical Pacific on equatorial variability. *Geophys. Res. Lett.,* **24,** 2589–2592.

Mantua, N. J., S. R. Hare, Y. Zhang, J. M. Wallace, and R. C. Francis, 1997: A Pacific interdecadal climate oscillation with impacts on salmon production. *Bull. Amer. Meteor. Soc.,* **78,** 1069–1079.

Miller, A. J., D. R. Cayan, T. P. Barnett, N. E. Graham, and J. M. Oberhuber, 1994: Interdecadal variability of the Pacific Ocean: Model response to observed heat flux and wind stress anomalies. *Climate Dyn.,* **9,** 287–302.

Nakamura, H., G. Lin, and T. Yamagata, 1997: Decadal climate variability in the North Pacific during the recent decades. *Bull. Amer. Meteor. Soc.,* **78,** 2215–2225.

Rasmusson, E. M., and T. C. Carpenter, 1982: Variations in tropical sea surface temperature and suface wind fields associated with the Southern Oscillation/El Niño. *Mon. Wea. Rev.,* **110,** 354–384.

——, P. A. Arkin, W.-Y. Chen, and J. B. Jallickee, 1981: Biennial variations in surface temperature over the United States as revealed by singular decomposition. *Mon. Wea. Rev.,* **109,** 587–598.

Smith, T. M., R. W. Reynolds, R. E. Livezey, and D. C. Stokes, 1996: Reconstruction of historical sea surface temperatures using empirical orthogonal functions. *J. Climate,* **9,** 1403–1420.

Thompson, D. W. J., and J. M. Wallace, 1998: The Arctic Oscillation signature in the wintertime geopotential height and temperature fields. *Geophys. Res. Lett.,* **25,** 1297–1300.

Tourre, Y. M., and W. B. White, 1995: ENSO signals in global upper-ocean temperature. *J. Phys. Oceanogr.,* **25,** 1317–1332.

Trenberth, K. E., and J. W. Hurrel, 1994: Decadal atmosphere–ocean variations in the Pacific. *Climate Dyn.,* **9,** 303–319.

Venegas, S. A., L. A. Mysak, and D. N. Straub, 1996: Evidence for interannual and interdecadal climate variability in the South Atlantic. *Geophys. Res. Lett.,* **23,** 2673–2676.

——, ——, and ——, 1997: Atmosphere–ocean coupled variability in the South Atlantic. *J. Climate,* **10,** 2904–2920.

Wallace, J. M., and D. S. Gutzler, 1981: Teleconnections in the geopotential height field during the Northern Hemisphere winter. *Mon. Wea. Rev.,* **109,** 784–812.

Zhang, R.-H., L. M. Rothstein, and A. J. Busalacchi, 1998: Origin of upper-ocean warming and El Niño change on decadal scales in the tropical Pacific Ocean. *Nature,* **391,** 879–883.

Zhang, Y., J. M. Wallace, and D. S. Battisiti, 1997: ENSO-like interdecadal variability: 1900–93. *J. Climate,* **10,** 1004–1020.